Simulating Ru L_3-Edge X-ray Absorption Spectroscopy with Time-Dependent Density Functional Theory: Model Complexes and Electron Localization in Mixed-Valence Metal Dimers

Benjamin E. Van Kuiken[†], Marat Valiev[‡], Stephanie L. Daifuku[†], Caitlin Bannan[†], Matthew L. Strader[§], Hana Cho[§], Nils Huse[§], Robert W. Schoenlein[§], Niranjan Govind[‡], and Munira Khalil[*†]

[†] Department of Chemistry, University of Washington, Seattle, Washington 98195, United States
[‡] William R. Wiley Environmental Molecular Sciences Laboratory, Pacific Northwest National Laboratory, Richland, Washington 99352, United States
[§] Ultrafast X-ray Science Laboratory, Chemical Sciences Division, Lawrence Berkeley National Laboratory, Berkeley, California 94720, United States

Abstract

Ruthenium L_3-edge X-ray absorption (XA) spectroscopy probes unoccupied 4d orbitals of the metal atom and is increasingly being used to investigate the local electronic structure in ground and excited electronic states of Ru complexes. The simultaneous development of computational tools for simulating Ru L_3-edge spectra is crucial for interpreting the spectral features at a molecular level. This study demonstrates that time-dependent density functional theory (TDDFT) is a viable and predictive tool for simulating ruthenium L_3-edge XA spectroscopy. We systematically investigate the effects of exchange correlation functional and implicit and explicit solvent interactions on a series of Ru^{II} and Ru^{III} complexes in their ground and electronic excited states. The TDDFT simulations reproduce all of the experimentally observed features in Ru L_3-edge XA spectra within the experimental resolution (0.4 eV). Our simulations identify ligand-specific charge transfer features in complicated Ru L_3-edge spectra of $[Ru(CN)_6]^{4-}$ and Ru^{II} polypyridyl complexes illustrating the advantage of using TDDFT in complex systems. We conclude that the B3LYP functional most accurately predicts the transition energies of charge transfer features in these systems. We use our TDDFT approach to simulate experimental Ru L_3-edge XA spectra of transition metal mixed-valence dimers of the form $[(NC)_5M^{II}\text{-}CN\text{-}Ru^{III}(NH_3)_5]^-$ (where M = Fe or Ru) dissolved in water. Our study determines the spectral signatures of electron delocalization in Ru L_3-edge XA spectra. We find that the inclusion of explicit solvent molecules is necessary for reproducing the spectral features and the experimentally determined valencies in these mixed-valence complexes. This study validates the use of TDDFT for simulating Ru 2p excitations using popular quantum chemistry codes and providing a powerful interpretive tool for equilibrium and ultrafast Ru L_3-edge XA spectroscopy.

1 Introduction

The structure, bonding, redox, and excited state properties of ruthenium complexes have been widely studied in recent years due to their applications as dye molecules for solar energy conversion and catalysts for efficient water splitting.(1-3) In each of these energy conversion applications it has been shown that the electronic structure of the Ru complex critically influences its function. It has become increasingly important to develop experimental probes capable of tracking the rearrangements of 4d electrons with high spatial and temporal resolution

in the ground and excited electronic states of Ru complexes. Ru L-edge X-ray absorption (XA) spectroscopy is dominated by excitations from Ru 2p orbitals to unoccupied orbitals with Ru 4d character and is a sensitive tool for understanding the detailed electronic structure of Ru compounds in disordered media. Recent equilibrium Ru L-edge XA measurements have investigated the electronic structure of water oxidation catalysts and enzyme mimics in the ground electronic state.(4, 5) Picosecond Ru L-edge XA spectroscopy has been used to characterize the transient excited states of Ru^{II} polypyridine complexes relevant to solar energy conversion.(6-8)

The interpretation of Ru L-edge XA spectra at a molecular level requires detailed simulations which relate the observed spectral features to the molecular electronic structure around the Ru atom. The most widely used approach for simulating the L-edges of molecular and solid state systems has been the semiempirical charge transfer multiplet (CTM) method developed by de Groot and co-workers and distributed as the CTM4XAS software package.(9) For Ru, this approach would treat only the 2p and 4d electrons explicitly by forming $2p^6 4d^N$ ground states and $2p^5 4d^{N+1}$ core-excited states from ligand field theory. The effects of covalent metal–ligand interactions that give rise to charge transfer (CT) features in L-edge XA spectra are accounted for by considering $4d^{N-1}L^1$ and $4d^{N+1}L^{-1}$ configurations in the valence space. These simulations require user input of ligand field parameters (such as Δ_0 for O_h symmetry), scaling factors by which Slater integrals and spin–orbit coupling differ from atomic values, and charge transfer energies for each system. Moreover, CTM calculations become quite complicated for low symmetry molecules where many ligand field and charge transfer parameters would be required. While these calculations provide great insight and offer a direct connection to ligand field models widely used in inorganic chemistry, they fail to be predictive because a new set of parameters is needed for each molecule. Consequently, it is desirable to have first principles quantum chemical tools that can interpret and predict L-edge XA spectroscopy.

Several recent papers have successfully simulated the Ru $L_{2,3}$-edge spectra of Ru complexes in solution by employing a molecular orbital approximation for core excitations.(4, 10) The orbitals used to determine the excitation energies and transition dipole moments are ground state relativistic spinor orbitals. This approximation has been quite successful in simulating the spectra of $[Ru(NH_3)_6]^{3+}$ and *cis,cis*-$[Ru_2O(OH_2)_2(bpy)_4]^{4+}$ called the "blue dimer." The disadvantage of this method is that it completely ignores final state effects, and relies on the orbital energy differences to give the excitation energies. The Z+1 approximation has been used with spin-free orbitals to simulate the L-edge spectra of $[Ru(bpy)_3]^{2+}$.(11) While this approach includes final state effects, it has been shown to worsen agreement with experiment in some cases.(10) Finally, we note that there are a number of other methods rooted in relativistic quantum chemistry that could potentially be used to simulate Ru L-edge XA spectra. These include the 4-component static exchange (STEX) approximation,(12) the ab initio multiplet method,(13) and relativistic TDDFT.(14-16) The disadvantages of these approaches may include the complexity and computational cost of 4-component calculations, reliance on HF theory, or implementations that are limited to closed-shell systems. Consequently, it is desirable to have a computational tool that is predictive and widely available.

In several recent works time-dependent density functional theory (TDDFT) has been employed to simulate Ru L_3-edge XA spectroscopy and has successfully reproduced all spectral features observed experimentally.(7, 10, 17) However, a comprehensive study of how various simulation

parameters affect the spectral features in the computed spectra is lacking. The goal of the present work is to provide a detailed characterization of applying TDDFT to simulate Ru L_3-edge XA spectroscopy. We begin by explaining that the effects of spin–orbit coupling (SOC) on the L_3-edges of Ru complexes are small compared to natural and experimental line broadening, which justifies the use of our spin-free (no SOC) TDDFT-based protocol for simulating Ru L_3-edge XA spectroscopy. We find that our computed spectra for a series of Ru^{II} and Ru^{III} complexes predict the experimental peak positions with a typical deviation of 0.26 eV. From these results, recommended simulation parameters are discussed, and the importance of choosing an appropriate exchange–correlation (XC) functional for the prediction of CT features is emphasized. In the context of this work, we adopt the language of transition metal L-edge spectroscopy where spectral features arising from the overlap of metal and ligand orbitals are termed CT features. Finally, the measured and simulated Ru L_3-edge XA spectra of mixed-valence transition metal complexes of the form, $[(NC)_5M^{II}\text{-}CN\text{-}Ru^{III}(NH_3)_5]^-$ where M = Fe and Ru (denoted $Fe^{II}Ru^{III}$ and $Ru^{II}Ru^{III}$), are presented. The XA spectra are consistent with localized charges on the metals. We discuss the importance of solvent models for understanding properties of transition metal complexes in solution, and we use explicit solvent models to show that the hydrogen bonding environment strongly stabilizes the $Fe^{II}Ru^{III}$ and $Ru^{II}Ru^{III}$ oxidations states. The mixed valence simulations highlight the predictive power of our approach for cases involving multiple metal centers and deviations from ideal symmetry.

2 Experimental Methods

$Ru(NH_3)_6Cl_3$ and $K_4Ru(CN)_6$ were purchased from Sigma Aldrich and used without further purification. $Fe^{II}Ru^{III}$ and $Ru^{II}Ru^{III}$ were prepared as their sodium salts according to literature methods and purified using a BioGel P2 column to remove starting materials from samples.(18) Samples for XA measurements were prepared by dissolving the molecules in water.

The XA measurements of $Ru(NH_3)_6Cl_3$, $K_4Ru(CN)_6$, $NaFe^{II}Ru^{III}$, and $NaRu^{II}Ru^{III}$ were performed on beamline 6.0.1 at the Advanced Light Source at Lawrence Berkeley National Laboratory. This beamline is equipped with a double crystal (Si) monochromator delivering monochromatic X-rays with ~0.4 eV resolution at the Ru L_3-edge (2840 eV). XA measurements were performed by monitoring the transmission of the X-rays through a ~100 μm film of the sample produced by the wire-guided jet in a helium atmosphere. This allowed the sample to be flowed continuously preventing X-ray damage. The monochromator energy was calibrated using the published data for $Ru(bpy)_3Cl_2$.(6)

3 Computational Methods

Geometry optimizations for all single valence molecules was performed with the ORCA quantum chemistry package.(19) Molecular geometries were optimized using the B3LYP functional.(20, 21) The def2-SV(P) basis set was used for the ligands, and the def2-SVP basis was used for Ru with the associated ECP.(22) The conductor-like screening model (COSMO) was used to model the solvent ($\varepsilon = 80.4$ and $n = 1.33$) environment and stabilize the anions.(23) The geometries of the $N3^{4-}$ dye were taken from our previous work.(7)

In the mixed quantum and molecular mechanical (QM/MM) simulations, the mixed-valence complexes comprised the QM region, and the solvent made up the MM region. The PBE0 functional was used for optimizations in the QM region.(24) It is noted that the use of PBE0 instead of B3LYP should not introduce significant systematic differences as both give reasonable geometric parameters for transition metal complexes. The 6-31G* basis set ligand atoms, and the

Stuttgart/Dresden ECPs were used for Ru and Fe in conjunction with the standard double-ζ basis sets.(25) $Fe^{II}Ru^{III}$ and $Ru^{II}Ru^{III}$ complexes were placed in 3 nm cubic solvent boxes with periodic boundary conditions and the SPC/E water model was used.(26) Following the initial solvation of the complexes, the MM region was optimized, and then the solvent was equilibrated for 100 ps. A constant temperature ensemble at 298.15 K was employed with a Berendsen thermostat.(27) The cutoff for electrostatic interactions was 1.5 nm. During the equilibration step, the QM solute was fixed and represented by a set of atom-centered point charges determined by fitting the electrostatic potential of the solute. The final configuration from the equilibration was taken, and a QM/MM optimization was performed. The latter involves relaxation of both quantum and classical regions. The optimized geometry was used to calculate the X-ray spectra of the mixed-valence species. Within harmonic approximation of solute–solvent fluctuations, such an approach typically provides reasonable values for the maxima of the absorption bands. More accurate calculation would involve full sampling of the entire system at finite temperature, but would be computationally prohibitive at this point. All QM/MM calculations were performed with NWChem.(28)

Linear-response TDDFT calculations were performed to model the Ru L_3-edge XA spectra by only looking for solutions to the TDDFT eigenvalue problem which involved single particle excitations from molecular orbitals with Ru 2p character. Scalar relativistic effects were accounted for by the second order Douglass-Kroll-Hess (DKH) Hamiltonian as implemented in ORCA.(29) The COSMO was used in all TDDFT calculations performed with ORCA. We note that effect of the continuum solvent on the excitation energies was insignificant. For XA calculations the def2-SV(P) was used for ligand atoms, and the def2-TZVP basis set was used for Fe. The SARC variant of these basis sets was used.(30) The all-electron Sapporo-DK-TZP basis was used for the Ru atom,(31) but the *g* functions were removed from this basis greatly increasing the stability of the SCF iterations. All of these basis sets have been optimized for use with relativistic Hamiltonians. The impact of XC functional on Ru L_3-edge XA spectra will be discussed in detail below. For the purposes of this study we have investigated the pure DFT functional BP.(32, 33) In addition, we investigated the TPSSh,(34) O3LYP,(35) B3LYP, and PBE0 functionals, which contain 10, 11.6, 20, and 25% HF exchange, respectively. TDDFT calculations were also performed using the QM/MM framework by including all classical point charges, and the restricted energy window (REW) approach recently implemented in NWChem.(17) These calculations employed the zeroth-order regular approximation (ZORA) to account for scalar relativistic effects.(36, 37) We note that the same basis sets and energy shifts (listed in Table 3) are applied for ZORA results. Spectral profiles for all simulated spectra are generated by convoluting the discrete excitations with Voigt profiles with natural (Lorentzian) and instrument (Gaussian) widths of 1.75 and 0.4 eV, respectively.

4 Results and Discussion

4.1 L-Edge Spectroscopy of Ru Complexes: Spin–Orbit and Multiplet Effects

Figure 1 demonstrates the effects of SOC on Ru $L_{2,3}$-edge spectra. It shows three ligand field multiplet simulations of Ru L_3-edge spectra for an octahedral Ru^{III} (d^5) complex with Δ_0 = 3.5 eV. The three cases considered are (i) inclusion of the atomic values of 2p and 4d SOC (blue traces), (ii) neglect of 4d SOC (green traces), and (iii) complete neglect of all SOC (solid and dotted black lines). Figure 1a shows the full L-edge spectrum arising from excitations involving

the 2p orbitals. In the cases with 2p SOC included (blue and green), there are features near 2840 and 2970 eV defined as the L_3- and L_2-edges. These features arise from $2p_{3/2} \rightarrow 4d$ and $2p_{1/2} \rightarrow 4d$ transitions, respectively. In the case of no SOC there is only a single feature arising from the Ru $2p \rightarrow 4d$ transitions.

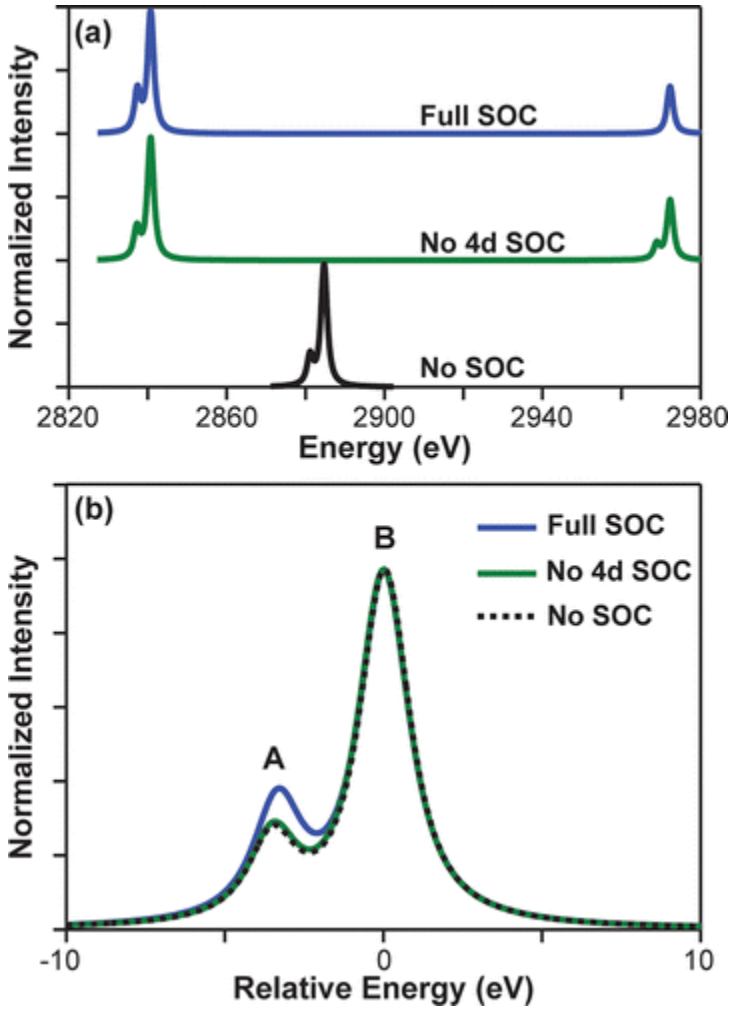

Figure 1. Ligand field multiplet calculations for an octahedral Ru^{III} complex with Δ_0 = 3.5 eV. The Slater integrals have been reduced to 25% of their atomic values. Spectra are shown for the L-edges arising from excitations from the 2p orbitals for three cases: full atomic SOC in the 2p and 4d orbitals (blue curves), no 4d SOC (green curves), and complete neglect of SOC (black curves). Panel a shows complete spectra, and panel b compares the lineshapes of the L_3-edges for each of the cases described above where feature B is centered at 0 eV. All spectra have been normalized to the intensity of the largest feature.

Figure 1b compares the L_3-edge spectra for the cases including 2p SOC with the spin-free simulation. This absorption edge contains two features labeled A and B. Since this is an octahedral complex, the Ru 4d orbitals will be split into t_{2g} end e_g orbitals by the ligand field with a low-spin $(t_{2g})^5(e_g)^0$ configuration. The allowed transitions at the Ru L_3-edge become $2p_{3/2} \rightarrow t_{2g}$ and $2p_{3/2} \rightarrow e_g$ for features A and B, respectively. The neglect of only 4d SOC results in a shift of −0.2 eV and a decrease in the relative intensity of the A feature arising from $2p_{3/2} \rightarrow t_{2g}$ transition. This has also been predicted for the Ru L-edge spectra of $[Ru(NH_3)_6]^{3+}$.(38) It is noted that the atomic SOC value has a greater magnitude than the ~0.1 eV extracted from experimental

data.(39) The spin-free spectrum is nearly indistinguishable from the case where only 4d SOC has been neglected. The similarity between the spin-free spectrum and the L_3-edges of spectra that include 2p SOC can be understood in terms of the selection rules of atomic spectroscopy. In the presence of SOC, one can consider the 4d orbitals to have either $4d_{5/2}$ (t_{2g}) or $4d_{3/2}$ (e_g) character. Transitions from the $2p_{3/2}$ level are allowed to each of the d orbitals by a $\Delta J = 0$ or ± 1 dipole selection rule.(39) In the case where SOC and configuration interaction are ignored, this reduces to the familiar $\Delta l = \pm 1$ dipole selection rule where p $\rightarrow$ d transitions are allowed. It should be noted that the effects of SOC are more pronounced at the L_2-edge. It is well documented that $2p_{1/2} \rightarrow t_{2g}$ ($4d_{5/2}$) transitions are dipole forbidden in octahedral complexes.(38, 39) This is evident in Figure 1a where the L_2-edge contains a single feature when 4d SOC is included (blue curve), but two features are present when 4d SOC is ignored (green curve). Additionally, the intensity branching ratios of the L-edges (defined as the ratio of the L_3-edge intensity to the total L-edge intensity) depend strongly on SOC and many-electron effects.(40) While we do not suggest that the L_2-edge should be ignored, we argue that much of the chemically relevant information contained in Ru L-edge XA spectroscopy can be extracted from the L_3-edge.

It is also important to consider the magnitude of multiplet effects in Ru L-edge XA spectroscopy. The overlap of 2p and valence d electrons show strong exchange interactions between ground and core-excited wave functions in transition metal complexes. As a result satellite features appear in L-edge spectra, and this phenomenon has been termed the multiplet effect. While multiplet effects typically dominate the 2p spectra of 3d transition metal complexes, the overlap of 2p and 4d orbital in Ru is small which diminishes these effects in Ru L-edge XA spectra.(41) Moreover, the 2p SOC in Ru complexes is large preventing the mixing of L_3- and L_2-edges. Recent molecular spinor calculations discussed in the introduction suggest that multiplet effects are relatively weak in Ru L_3-edge spectroscopy.(4) Based on the above discussion, we expect spin-free TDDFT to duplicate all of the experimentally resolved fine structure in Ru L_3-edge XA spectroscopy and provide a molecular level description of the various spectral features. These assumptions should also hold for other 4d metals and molecules that deviate from octahedral symmetry.

4.2 Experimental Spectra of Ru^{II} and Ru^{III} Complexes

The aqueous Ru L_3-edge XA spectra of $[Ru(NH_3)_6]^{3+}$, $[Ru(CN)_6]^{4-}$, $Fe^{II}Ru^{III}$, and $Ru^{II}Ru^{III}$ are presented in Figure 2a–d. The labeled spectral features have been determined by fitting Voigt profiles to the data, and their positions are listed in Tables 1 and 2. For the Ru^{III} complex, $[Ru(NH_3)_6]^{3+}$ shown in Figure 2a there are two spectral features labeled A (2837.3 eV) and B (2841.0 eV). With the Ru^{II} complex ($[Ru(CN)_6]^{4-}$) in Figure 2b, we identify two features in the pre-edge region of the XA spectrum labeled B (2841.4 eV) and C (2843.2 eV). Figure 2c shows the spectrum of the $Fe^{II}Ru^{III}$ dimer, which resembles the $[Ru(NH_3)_6]^{3+}$ spectrum with features A and B. The spectrum of $Ru^{II}Ru^{III}$ is shown in Figure 2d and contains A, B, and C features. Discussion of the XA spectra and chemistry of the mixed-valence complexes will be addressed in section 4.5. Here, we focus our attention on the spectra of $[Ru(NH_3)_6]^{3+}$ and $[Ru(CN)_6]^{4-}$, which represent typical Ru^{III} and Ru^{II} compounds. The L_3-edge spectra of these molecules contain features representative of a broad range of Ru complexes as we discuss below.

Table 1. Positions of Spectral Features A, B, and C (in eV) from Experimental Measurements and B3LYP Simulations of the Ru L_3-Edge XA Spectra Shown in Figures 2 and 3[a]

	A		B		C	
molecule	**calc.**	**exp.**	**calc.**	**exp.**	**calc.**	**exp.**
$[Ru(NH_3)_6]^{2+}$			2839.5			
$[Ru(NH_3)_6]^{3+}$	2836.8	2837.3[b]	2841.0	2841.0[b]		
$[RuCl_6]^{4-}$			2838.0			
$[RuCl_6]^{3-}$	2837.1	2838.2[c]	2839.5	2840.2[c]		
$[Ru(CN)_6]^{4-}$			2841.7	2841.4[b]	2843.4	2843.2[b]
$[Ru(CN)_6]^{3-}$	2836.8		2842.4		2844.9	
$^1A_1$ $[Ru(bpy)_3]^{2+}$			2840.6	2840.5[d]		
^{3}MLCT $[Ru(bpy)_3]^{2+}$	2837.1	2837.6[d]	2841.4	2841.4[d]		
$^1A_1$ $N3^{4-}$			2840.6	2840.3[e]	2843.6	2843.5[e]
^{3}MLCT $N3^{4-}$	2837.6	2837.5[e]	2841.3	2841.3[e]	2844.7	2844.9[e]

[a]A −2.49 eV shift is applied to the calculated spectra. The peak positions are determined by fitting Voigt profiles to the XA lineshapes.
[b]This work.
[c]Reference 46.
[d]Reference 6.
[e]Reference 7.

Table 2. Positions of Experimental and Calculated Spectral Features (in eV) Found in Ru L_3-Edge XA Spectra of the Mixed-Valence Metal Dimers, $Fe^{II}Ru^{III}$ and $Ru^{II}Ru^{III}$[b]

	A	B	C
$Fe^{II}Ru^{III}$			
experiment	2837.3	2841.0	
vacuum		2839.7	
COSMO		2840.0	
shell	2836.8	2841.1	
QM/MM	2836.9	2841.0	
$Ru^{II}Ru^{III}$			
experiment	2837.4	2841.2	2843.2
vacuum	2836.8	2839.7	2842.9
COSMO	2837.1	2840.8 (2842.5)[a]	2844.0
shell	2836.8	2841.3	2843.5
QM/MM	3837.0	2841.2	2843.6

[a]An additional feature was fit to the COSMO spectrum of $Ru^{II}Ru^{III}$ where the spectrum contains four distinguishable features.
[b]The peak positions are determined by fitting Voigt profiles to the XA lineshapes.

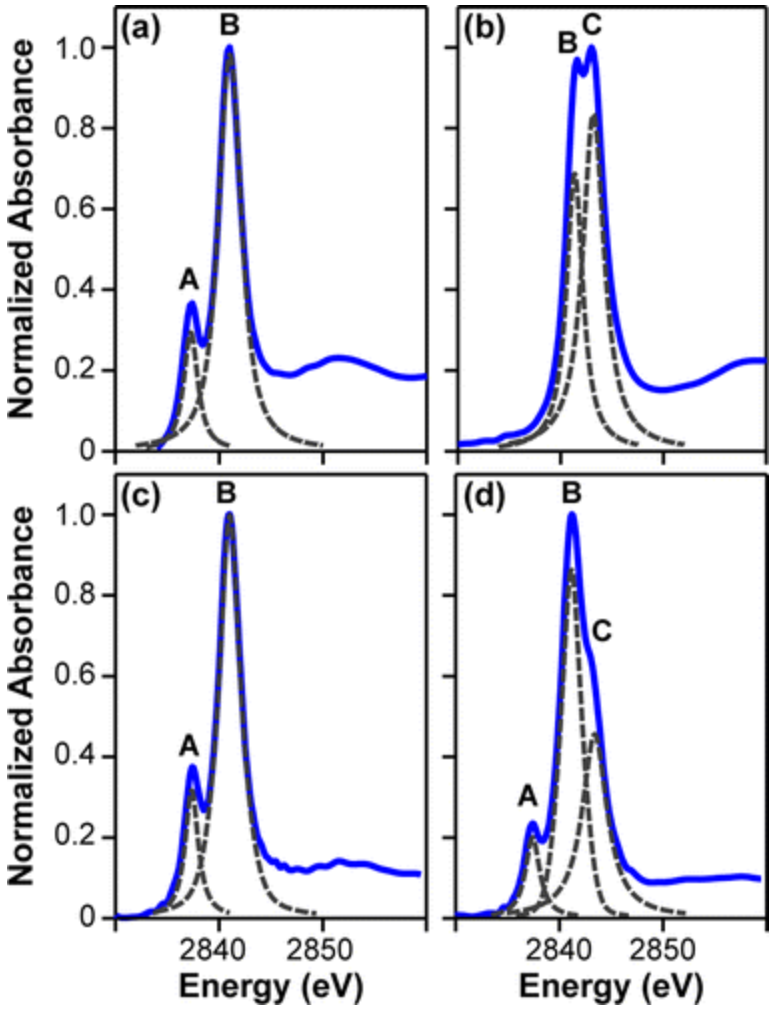

Figure 2. Experimental Ru L_3-edge XA spectra of aqueous solutions of (a) $Ru(NH_3)_6Cl_3$, (b) $K_4Ru(CN)_6$, (c) $Fe^{II}Ru^{III}$, and (d) $Ru^{II}Ru^{III}$. The maxima of the spectra have been normalized to unity. Near-edge features in the spectra are labeled A-C, and the positions have been determined by fitting Voigt profiles to the experimental data, which are shown as dashed gray curves. The positions of these features are reported in Tables 1 and 2.

As previously discussed, ligand field theory is commonly used to assign features in L-edge X-ray absorption spectroscopy. In O_h symmetry, the Ru 4d orbitals are split by the ligand field into two sets of orbitals where the triply degenerate t_{2g} set is stabilized below the doubly degenerate e_g orbitals by the ligand field splitting energy, Δ_0. For Ru^{II} complexes, there are six 4d electrons occupying a low-spin configuration, $(t_{2g})^6(e_g)^0$. In contrast, the Ru^{III} oxidation state has a $(t_{2g})^5(e_g)^0$ configuration. With this in mind, feature A in the Ru L_3-edge spectrum of $[Ru(NH_3)_6]^{3+}$ has been assigned to $2p_{3/2} \rightarrow t_{2g}$ transitions, and feature B is assigned to $2p_{3/2} \rightarrow e_g$ transitions. In a static orbital picture, the A-B splitting of 3.3 eV reports directly on the Δ_0 value. In the case of $[Ru(CN)_6]^{4-}$, one might expect transitions to only the vacant e_g orbitals (feature B), but we clearly see another strong spectral feature, labeled C in Figure 2b. We attribute the C feature to Ru $2p_{3/2} \rightarrow CN^-$ π^* transitions and will discuss in detail below how TDDFT is instrumental in identifying and assigning these charge-transfer excitations. Solomon and co-workers have assigned higher energy spectral features in the Fe $L_{2,3}$-edge XA spectra of

$[Fe^{II/III}(CN)_6]^{4-/3-}$ to charge transfer satellites arising from strong interactions with the CN^- π orbitals using ligand-field theory.(42)

4.3 TDDFT Simulations of Ru L_3-Edge XA Spectra of Model Complexes: Oxidation State and Ligand Field Effects

The Ru L_3-edge X-ray absorption spectra of $[Ru(NH_3)_6]^{2+/3+}$, $[RuCl_6]^{4-/3-}$, $[Ru(CN)]^{4-/3-}$, $^1A_1$ and ^{3}MLCT states of $[Ru(bpy)_3]^{2+}$, and $^1A_1$ and ^{3}MLCT states of $[Ru(dcbpy)_2(NCS)_2]^{4-}$ ($N3^{4-}$) are simulated with the B3LYP functional and shown in Figure 3. The positions of spectral features have been determined by fitting the sum of a Gaussian and Lorentzian function to each of the peaks in the spectrum, and their positions are listed in Table 1. We have applied a functional specific shift listed in Table 3 to each of the calculated spectra. The shift is determined by aligning the B feature in each calculated $[Ru(NH_3)_6]^{3+}$ spectrum to the position of the experimental peak labeled B in Figure 2a. The B feature of $[Ru(NH_3)_6]^{3+}$ was chosen for calibration because the simulated spectra do not change qualitatively with the functional choice for $[Ru(NH_3)_6]^{3+}$ (see Figure 6). We note that due to deficiencies in the XC functionals and neglect of SOC, unshifted energies are not expected to agree with experiment, and a constant energy shift is routinely applied in XA simulations.(43-45) The shifts in Table 3 provide a calibration energy for each functional. We do not discuss spectral features above the edge jump such as the feature near 2847 eV shown in the simulated $[RuCl_6]^{4-}$ spectrum in Figure 3. This is because these features appear at energies that are near or above the absorption edge and are likely artifacts of the finite basis set employed in our calculations.

Table 3. Energy Shifts for Each Functional Required to Align the B Feature of Calculated Spectra with the B Peak in the Experimental $[Ru(NH_3)_6]^{3+}$ Ru L_3-Edge XA Spectrum[a]

functional	energy shift (eV)
BP	17.19
O3LYP	3.03
TPSSh	5.93
B3LYP	–2.49
PBE0	–6.27

[a]The functionals are arranged in increasing order of HF content.

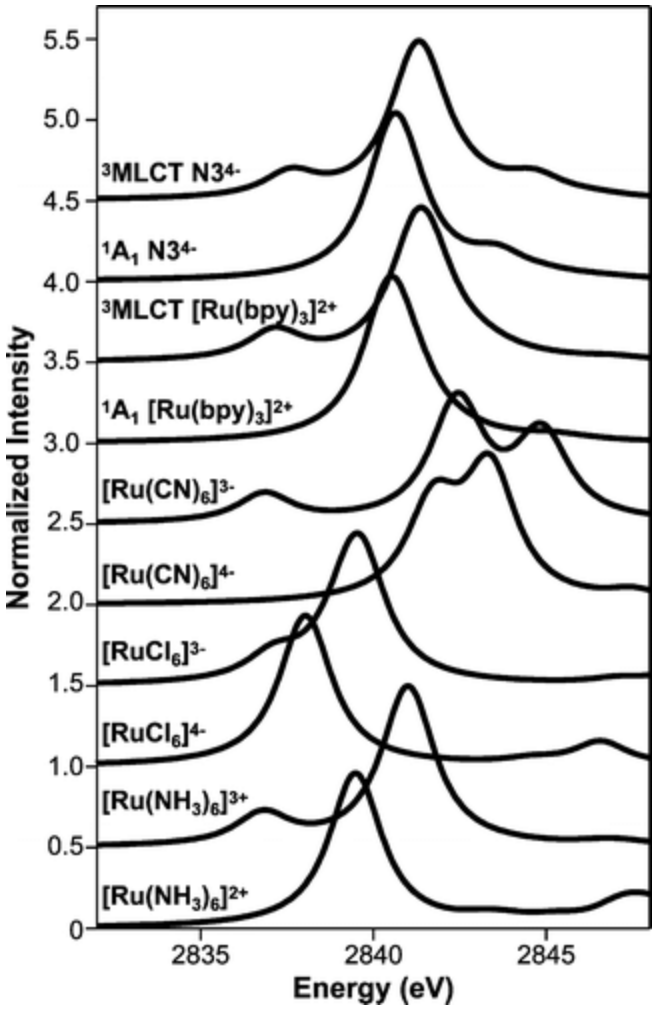

Figure 3. TDDFT spectra of the Ru complexes calculated with the B3LYP functional. The spectral profiles are generated by convoluting the discrete transitions with Voigt profiles of 0.4 eV Gaussian and 1.75 eV Lorentzian widths. The intensity of each spectrum is normalized to the most intense feature and it is vertically offset by 0.5 from the preceding spectrum. The spectral positions are listed in Table 1.

For a qualitative interpretation of the spectral features shown in Figure 3, we plot the positive part of the difference density for a transition giving rise to a particular spectral feature in the Ru L_3-edge XA spectrum in Figure S1 of the Supporting Information. The difference density is defined as the electron density of the excited state less the ground state density. It is a useful way to visualize core excitations when no single valence orbital characterizes the final state. The difference densities confirm that the TDDFT interpretations of the spectra agree with the ligand field description discussed in section 4.2, and the labels A, B, and C are used throughout this work to describe transitions of 2p → t_{2g}, 2p → e_g, and 2p → ligand π^* character, respectively.

The B3LYP functional does an excellent job of reproducing the experimentally observed energy splitting between spectral features and shifts in the spectra (see Table 1). Following the −2.49 eV shift, experimental peak positions are plotted against calculated values in Figure 4. The linear fit of these data yields a correlation coefficient of 0.991, and the root-mean-square deviation for the data is 0.26 eV, which is significantly less than the lifetime (1.75 eV) and instrument (0.4 eV)

widths at the Ru L_3-edge. We note that we have chosen to exclude the $[RuCl_6]^{3-}$ data from Figure 4.(46) For the case of $[RuCl_6]^{3-}$, the A feature deviates by +1.1 eV from the experimental value and the B feature deviates by +0.7 eV, which is significantly greater than the RMSD of 0.26 eV. We consider $[RuCl_6]^{3-}$ to be a clear outlier, and this is likely due to the fact that the experiment used a separate energy calibration from the spectra that we have measured. However, we note that including the $[RuCl_6]^{3-}$ data in the theory—experiment comparison still yields a reasonable correlation coefficient of 0.97. Most importantly, the result in Figure 4 clearly shows that TDDFT calculations employing the B3LYP functional are capable of reproducing each of the major features observed in the experimental Ru L_3-edge spectra for all the Ru complexes considered in this study.

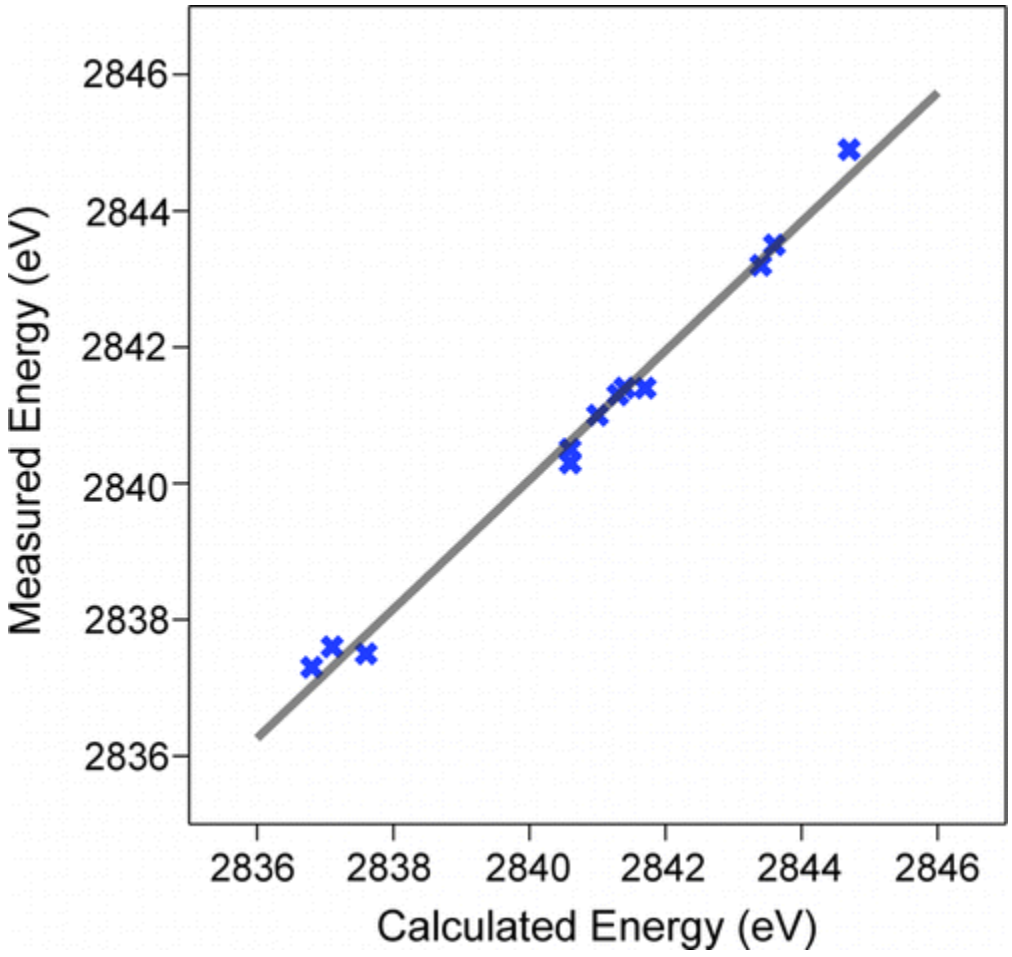

Figure 4. Comparison of the energies of fitted spectral features in calculated (after shift is applied) and measured Ru L_3-edge XA spectra for $[Ru(NH_3)_6]^{3+}$, $[Ru(CN)_6]^{4-}$, $[Ru(bpy)_3]^{2+}$, and $[Ru(dcbpy)_2(NCS)_2]^{4-}$($N3^{4-}$). The linear regression is shown as a dark gray line, and the correlation coefficient is 0.991. The RMSD for the data is 0.26 eV.

Having calibrated our calculations, several clear trends can be observed from the computed spectra in Figure 3. As mentioned above, the presence of the A feature in the spectra is a clear indication of an unfilled t_{2g} band and, in the series of complexes studied here, a Ru^{III} oxidation state of the metal. In addition to the appearance of the A feature; there is a shift of the B feature to higher energy for the Ru^{III} complexes. This increase in the transition energy is largely the

result of the energetic shifts of the Ru 2p orbitals upon oxidation. The average of the 2p orbital energy shifts by −4.0, −2.5, and −3.2 eV for the ammine, cyanide, and chloride complexes respectively upon oxidation of the Ru metal. The 2p orbital energies of $[Ru(bpy)_3]^{2+}$ and $N3^{4-}$ shift by −2.0 and −1.5 eV upon formation of the ^{3}MLCT state. In the case of $[Ru(bpy)_3]^{2+}$ and $N3^{4-}$ the calculated shifts of the 2p orbital energies agree well with the experimental changes of the ionization potentials of −1.8 and −2.0 eV, respectively.(6, 7) Our results emphasize the importance of accounting for shifts in the core orbitals when interpreting changes in Ru L-edge XA spectroscopy. Finally, we note that ligand field strengths are also evident in the spectra shown in Figure 3. In the case of the Ru^{III} complexes, the energy difference between the A and B features (E_{BA}), gives the ligand field energy within a single particle approximation. Our B3LYP calculations predict an increasing E_{BA} of 2.3, 4.2, and 5.6 eV for the Cl^-, NH_3, and CN^- ligands, respectively.

4.4 Charge Transfer Transitions and Functional Choice in Ru L-Edge XA Spectroscopy

One advantage of using quantum chemical methods to simulate XA spectroscopy is that they include all the chemical details of the molecules. While a strong CT feature was easily identified in the spectrum of $[Ru(CN)_6]^{4-}$, weak CT features vary greatly in intensity and may be ligand specific. Figure 5 shows the simulated Ru 2p spectrum of the $^1A_1$ state of the $N3^{4-}$ molecule that contains both bpy and NCS^- ligands. In this case, there are spectral features arising from transitions involving the Ru 2p orbitals to valence orbitals of Ru e_g, bpy π*, and NCS^- π* character with the two apparent features (B and C) being attributed to the Ru e_g and NCS^- π* character, respectively. Excitations to the Ru e_g, bpy π*, and NCS^- π* orbitals represent 75%, 14%, and 11% of the total integrated area of the Ru L_3-edge spectrum. The e_g and NCS^- features are centered at 2840.6 and 2843.6 eV and are shifted less than 0.1 eV from the positions of the B and C features that were determined by fitting two features to the spectral envelope. Table 1 lists the positions of the experimental and computed spectral features in the L_3-edge XA spectrum of $N3^{4-}$. The photochemistry and Ru L_3-edge XA spectroscopy of this complex has been discussed in detail in our previous work.(7) We include the $N3^{4-}$ example here to highlight the ability of TDDFT to reproduce spectral features and identify contributions from different ligands in low symmetry complexes. The simulated Ru L_3-edge spectrum of the $^1A_1$ state of $[Ru(bpy)_3]^{2+}$ (plotted in Figure 3) also exhibits a 14% intensity contribution from Ru 2p → bpy π* transitions.

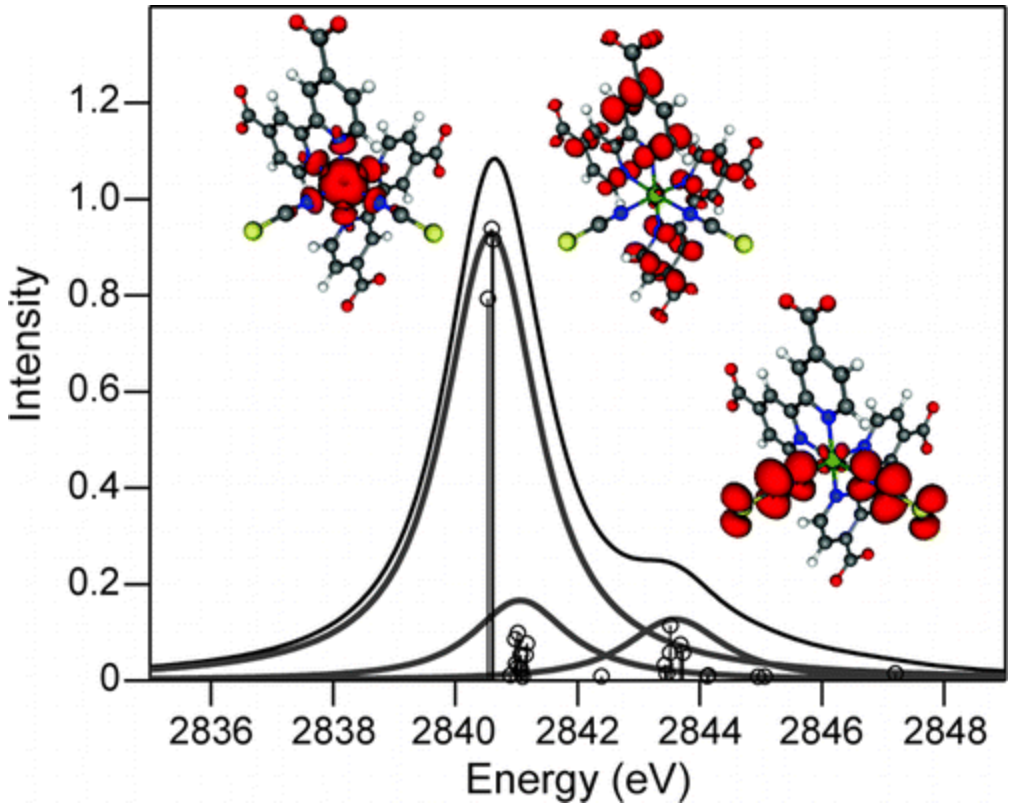

Figure 5. TDDFT B3LYP spectrum of the Ru L_3-edge of the $^1A_1$ state of $[Ru(dcbpy)_2(NCS)_2]^{4-}$($N3^{4-}$). The total spectrum is shown as a black solid line while contributions from transitions of 2p → Ru e_g, 2p → bpy, and 2p → NCS^- π* character are shown as gray curves. Difference densities representative of the features are shown with an isovalue of 0.002.

Figure 6 shows the Ru L_3-edge spectra of $[Ru(NH_3)_6]^{3+}$ and $[Ru(CN)_6]^{4-}$ calculated with BP, TPSSh, B3LYP, and PBE0 XC functionals. The experimental spectra are shown in the lower panels for comparison. In the case of $[Ru(NH_3)_6]^{3+}$ the spectra show little variation with change of functional. The most significant difference is in the energy splitting between the A and B features (E_{BA}). In particular, the BP functional underestimates the experimental E_{BA} value of 3.7 by 0.3 eV. All global hybrid functionals overestimate the E_{BA} experimental value resulting in calculated E_{BA} values of 4.0, 4.2, and 4.1 eV for TPSSh, B3LYP, and PBE0, respectively. In the case of $[RuCl_6]^{3-}$ the calculated E_{BA} is 1.5 and 2.3 eV for the BP and B3LYP functionals, respectively. The experimental E_{BA} value of $[RuCl_6]^{3-}$ is measured to be 2.0 eV which suggests that the global hybrid functionals are better at predicting the spin-free properties of these simple octahedral complexes, since an overestimation of E_{BA} is expected when SOC is not included.

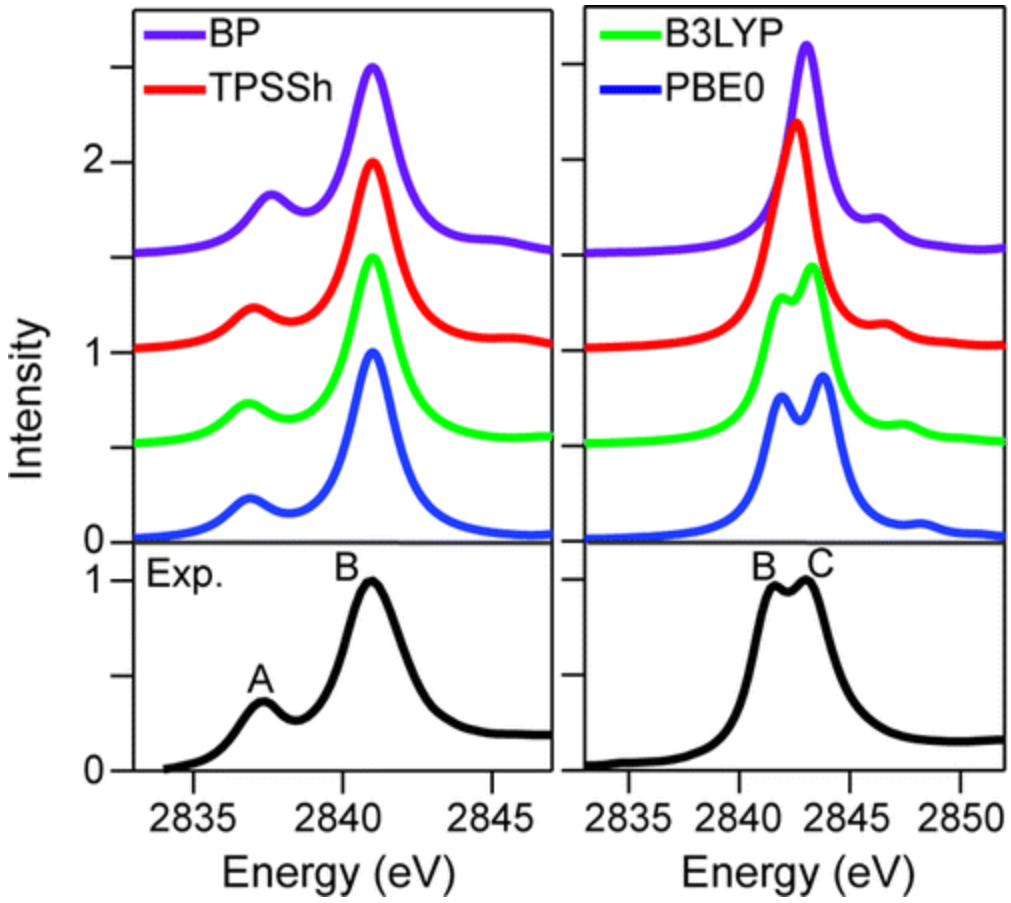

Figure 6. TDDFT spectra of the Ru L_3-edge of $[Ru^{III}(NH_3)_6]^{3+}$ (left) and $[Ru^{II}(CN)_6]^{4-}$ (right) calculated with BP, TPSSh, B3LYP, and PBE0 functionals. The bottom panel shows the experimental spectra for comparison.

In the case of $[Ru(CN)_6]^{4-}$ shown in Figure 6 (right column), the effect of HF exchange present in global hybrid functionals is much more apparent due to the presence of the CT feature, C. With no HF exchange contribution (the BP case) the B and C features have coalesced into a single peak and no charge transfer feature is visible. With 10% HF exchange, the spectrum begins to show two features and fitting the spectrum yields an energy difference between the B and C features of 1.0 eV. B3LYP and PBE0 give an energy difference between the B and C features of 1.7 and 2.0 eV, respectively, and are in good agreement with the experimental value of 1.8 eV.

To further assess the effect of HF exchange across a range of transitions, we consider the CT features present due to π^* orbitals of CN^- in $[Ru(CN)_6]^{3-/4-}$, NCS^- in $N3^{4-}$, and bpy in $[Ru(bpy)_3]^{2+}$ and $N3^{4-}$. We focus on the relative CT energy defined as the energy difference between the most intense CT transition and the most intense e_g transition and plot it against the percent of HF exchange in Figure 7. In all cases the relative CT energy increases with the HF exchange content. Transitions arising from CN^- π^* orbitals (blue crosses and red circles) have the weakest dependence on HF exchange while the features arising from bpy ligands (black asterisks and magenta plus signs) have the strongest dependence. The strong dependence of the bpy CT states on the HF exchange content is expected due to the diffuse nature of bpy π^* orbitals involved in these excitations as shown in the difference densities plotted in Figure 5. Use of a pure DFT functional like BP produces a feature that is >2.0 eV below the e_g feature yielding a

low energy peak in the XA spectrum that is not observed experimentally. The weak dependence of the CN^- π^* transitions on the functional choice results from the larger metal character in the CT state due to strong metal–ligand interactions.

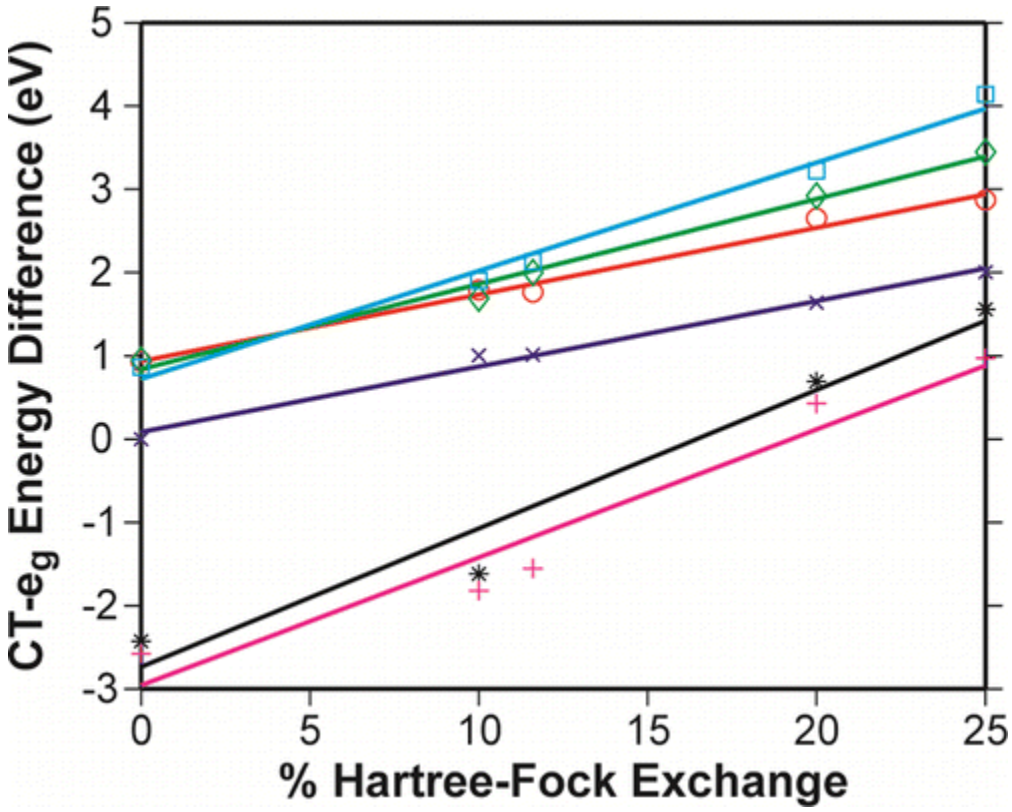

Figure 7. Difference between the energy of the most intense CT transition and most intense e_g transition is shown as a function of the HF exchange contribution to the functional. Data is shown for the CN^- peak of $[Ru(CN)_6]^{4-}$ (blue crosses) and $[Ru(CN)_6]^{3-}$ (red circles), the NCS^- peak of $^1A_1$ $N3^{4-}$ (green diamonds) and ^{3}MLCT $N3^{4-}$ (cyan squares), and the bpy peak of $[Ru(bpy)]^{2+}$ (black asterisks) and $^1A_1$ $N3^{4-}$ (magenta plus symbol). Linear fits to the data provide a visual guide.

Based on the above observations, it appears that the B3LYP and PBE0 functionals are able to predict the energies of CT features in Ru L-edge spectroscopy. However, PBE0 consistently overestimates the energy of CT features, and the RMSD for the difference between experiment and theory is 0.44 eV, which is significantly greater than the RMSD of 0.26 eV for B3LYP. If the linear regressions in Figure 7 are used to determine the optimal values of HF exchange, it is predicted that 22%, 21%, and 22% would produce the experimentally observed CT energies for $[Ru(CN)_6]^{4-}$, $^1A_1$ $N3^{4-}$, and ^{3}MLCT $N3^{4-}$, respectively. Thus, we conclude that B3LYP with 20% HF exchange provides the best choice for XC functional among the set of commonly used functionals that we have investigated. The importance of using global hybrid functionals for TDDFT simulations of XA spectra has been previously discussed for the pre-edge region of transition metal K-edge spectroscopy. We observed that use of the BP functional leads to underestimation of Fe 1s → ligand π^* transition energies in an Fe^{II} spin crossover complex.(47) In the recent work of Roemelt et al. a functional with 22% HF exchange was recommended for reproducing the pre-edge spectra of Mn complexes where Mn 1s → 3d transitions and Mn 1s → π^* CT transitions are important.(48) These studies are in agreement with our present results and

provide additional evidence that B3LYP is a reliable functional for TDDFT simulations of core-level spectroscopies in these systems. The above discussion suggests that the observed CT features are not long-range excitations. Consequently, sophisticated range-separated hybrid functionals are not required to reproduce energies of the CT features in Ru L-edge XA spectroscopy.

4.5 Ru L-Edge XA Spectroscopy of Cyanide Bridged Mixed-Valence Metal Dimers

The spectroscopy of transition metal mixed-valence complexes has garnered much interest because they provide ideal systems for understanding coupled electronic and nuclear motions during ultrafast photoinduced metal-to-metal charge transfer (MMCT).(49-54) We study cyanide-bridged dimer systems of the form, $[(NC)_5M^{II}\text{-}CN\text{-}Ru^{III}(NH_3)_5]^-$, where M = Fe or Ru. One of the important questions in the chemistry of mixed-valence molecules is of electron delocalization.(55) While the formal charges of metals in $Fe^{II}Ru^{III}$ complex suggest d^6 and d^5 ground state electron configurations, electronic coupling between the metal centers can lead to electron delocalization across the cyanide bridge and result in deviations to the formal charges.(55) This has important implications for understanding the MMCT process, since electron delocalization modifies the charge transfer distance and solvent dipole orientation. The solvent itself has a strong impact on the degree of localization, which is evidenced by the solvatochromism of the MMCT energy in the visible and NIR.(56) Given that Ru L-edge XA spectroscopy is sensitive to the oxidation state of Ru complexes, we use it to measure the degree to which the charges are delocalized in $Fe^{II}Ru^{III}$ and $Ru^{II}Ru^{III}$. Moreover, these complexes provide a useful test case for assessing the level of detail that must be employed to treat solvent effects in computational models for effectively simulating core-level XA spectra.

For modeling the solvent, we have employed both implicit and explicit solvent models and compared these to the gas phase results. For the implicit solvent the COSMO model has been used. For explicit modeling of the solvent, the QM/MM protocol described in section 2 was used. An additional solvent model, which we call the "shell" model, was constructed by extracting the solute and the first solvation shell from the QM/MM simulation box. In this study it includes the twenty-six water molecules nearest to the solute (within ~2.3 Å of the solute). For the shell model, the entire system is treated quantum mechanically, and the rest of the solvent is treated with COSMO. The shell model allows us to calculate the X-ray spectrum with ORCA providing an implementation independent comparison with other results. Regardless of solvent treatment the same geometry from the QM/MM optimization is employed for all X-ray simulations. The octahedra of the two metals are aligned and the molecule is bent so hydrogen bonds form between the cyanide and ammine groups (see Figure S2). These bent structures are qualitatively similar to the crystal structure of a related iron–ruthenium dimer.(57) This geometry is also similar to the bent COSMO optimized geometry reported by Kondov et al.(58) Linear geometries that likely exist in solution were also investigated, but little difference was observed between the X-ray spectra of linear and bent species. A future study will investigate the role of structural heterogeneity on the spectroscopic properties of these molecules. Inspection of the QM/MM geometries show that there are many hydrogen bonds to the cyanide ligands while the NH_3 ligands are not as strongly coordinated by the surrounding solvent.

Figure 8 shows the experimental and simulated (using B3LYP) XA spectra of the Ru L_3-edge of $Fe^{II}Ru^{III}$. The spectral positions for the peaks in the experimental and computed XA spectra are

listed in Table 2. The green shaded area represents the spectrum of $[Ru(NH_3)_6]^{3+}$. The similarity between the $Fe^{II}Ru^{III}$ spectrum and the green shaded area suggests that the Ru atom in $Fe^{II}Ru^{III}$ is in the +3 oxidation with similar character to Ru in $[Ru(NH_3)_6]^{3+}$. The simulated spectra for the gas phase and COSMO models contain only a single feature centered at 2839.7 and 28340.0 eV. The B feature in the simulated $[Ru(NH_3)_6]^{2+}$ spectrum lies at 2839.5 eV suggesting that the gas phase and COSMO results predict that the Ru atom in $Fe^{II}Ru^{III}$ is in the +2 oxidation state. This conclusion is supported by the Mulliken spin populations reported in Table 4 confirming presence of the unpaired electron on the Fe atom. Conversely, use of either of the explicit solvent models reproduces the double peaked spectrum observed experimentally, and the spin populations of 0.0 on Fe and 1.0 on Ru confirm the presence a localized unpaired electron on the Ru center. This strongly supports the interpretation of $Fe^{II}Ru^{III}$ valencies with localized d electrons.

Table 4. Mulliken Spin Population on Each of the Metal Centers for Each Solvent Treatment Used to Calculate Ru L_3-Edge XA Spectra of the Mixed Valence Complexes, $Fe^{II}Ru^{III}$ and $Ru^{II}Ru^{III}$[a]

	$Fe^{II}Ru^{III}$		**$Ru^{II}Ru^{III}$**	
	Fe	**Ru**	**Ru[CN]**	**Ru[NH_3]**
vacuum	1.11	–0.01	0.87	0.00
COSMO	1.00	0.11	0.24	0.75
shell	0.00	1.04	0.00	1.04
QM/MM	0.04	0.97	0.03	0.98

[a]Ru[CN] and Ru[NH_3] refer to the Ru atom in the $Ru(CN)_6$ and $Ru(NH_3)_5$ moieties, respectively.

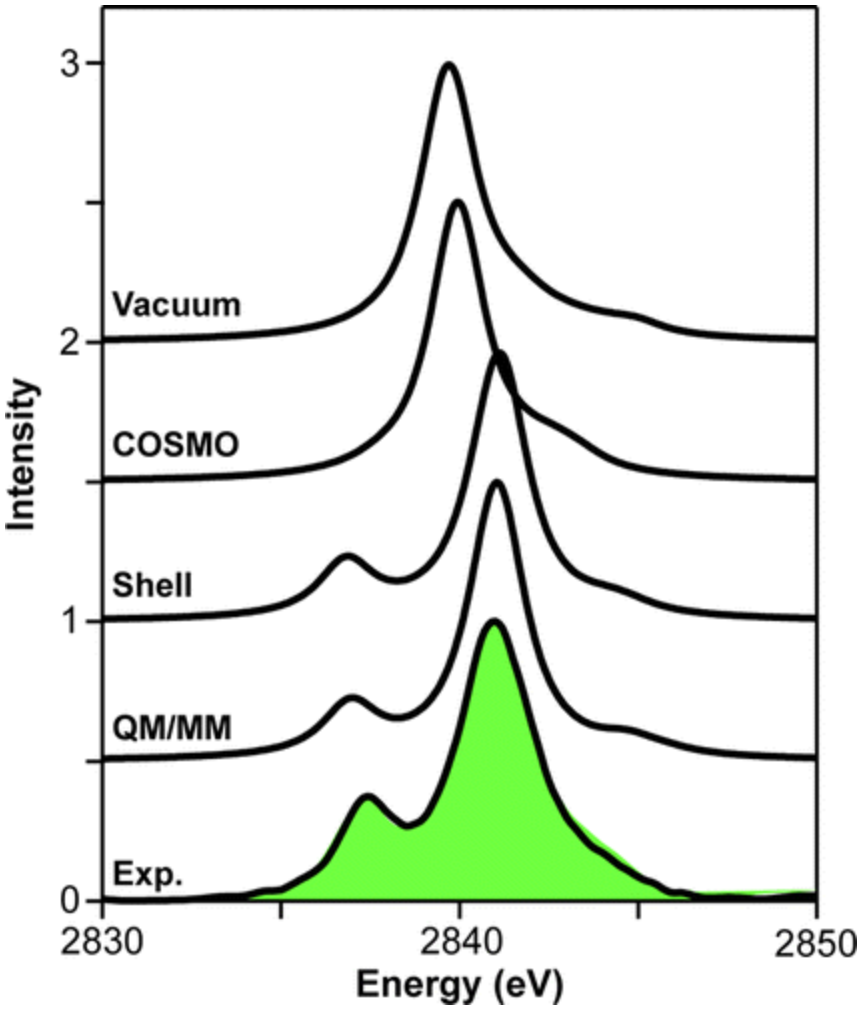

Figure 8. Experimental and simulated Ru L_3-edge spectra of $Fe^{II}Ru^{III}$. The experimental spectrum is shown following subtraction of the edge jump. The green shaded region represents the $[Ru(NH_3)_6]^{3+}$ spectrum. Simulated spectra are shown for vacuum (gas phase), COSMO, shell, and QM/MM treatments of the solvent environment as described in the main text. The maximum of each spectrum has been normalized to 1.0.

As shown previously in Figure 2d, the experimental Ru L_3-edge XA spectrum for the $Ru^{II}Ru^{III}$ complex contains three features labeled A, B, and C. The summation of the experimental $[Ru(NH_3)_6]^{3+}$ and $[Ru(CN)_6]^{4-}$ XA spectra is shown as the green shaded area in Figure 9a and it does an excellent job of reproducing the experimentally measured $Ru^{II}Ru^{III}$ spectrum (bottom curve). While there are slight differences in intensities of the spectral features between the summed and $Ru^{II}Ru^{III}$ spectra, their positions are not shifted significantly. The simulated $Ru^{II}Ru^{III}$ spectra shown in Figure 9a are broader than the experimental spectra but show three features in the case of the shell and QM/MM models.

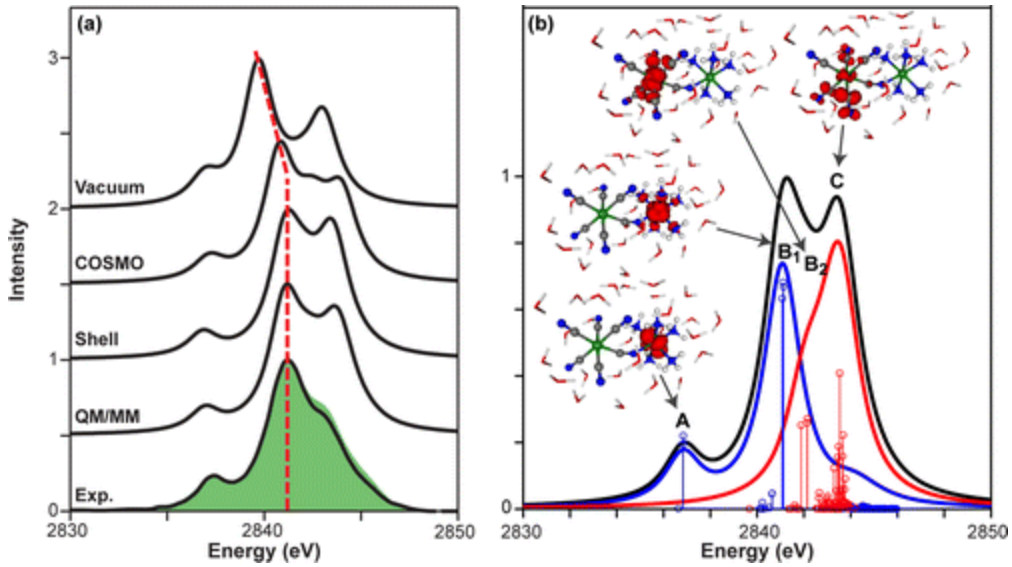

Figure 9. (a) Experimental and B3LYP TDDFT Ru L_3-edge XA spectra of $Ru^{II}Ru^{III}$. The experimental spectrum is shown following subtraction of the edge jump. The green shaded region represents the normalized summation of experimental $[Ru(NH_3)_6]^{3+}$ and $[Ru(CN)_6]^{4-}$ spectra. Simulated spectra are shown for vacuum, COSMO, shell, and QM/MM treatments of the solvent environment as described in the main text. The maximum of each spectrum has been normalized to 1.0. Red dotted line is to guide the eye on the position of the most intense feature identified as the $Ru[NH_3]$ 2p → e_g transition. (b) B3LYP spectrum of $Ru^{II}Ru^{III}$ using the shell model for the solvent. Individual contributions from the $Ru[NH_3]$ and Ru[CN] fragments are shown as blue and red data, respectively. Difference densities (isovalues of 0.005) identify the contributions to the spectra.

To identify the individual contributions to the spectra, the B3LYP spectrum of $Ru^{II}Ru^{III}$ simulated with the shell model is plotted in Figure 9b. The blue and red data show the contributions from the individual fragments, and four contributions to the spectrum are identified. The total spectrum contains excitations from the $Ru[NH_3]$ fragment where core-excited states are characterized by excitation into t_{2g} (A) and e_g (B_1) orbitals and the Ru[CN] fragment with core excitations to e_g (B_2) and CN^- π^* (C) orbitals. Despite containing each contribution observed in the spectra of the model complexes, the spectrum of Ru[CN] shown in red has a different intensity pattern than the spectrum of the model complex where each feature (B and C in Figure 2b) has nearly equal intensity. The low intensity of the B_2 feature relative to the C feature could account for the discrepancy between the measured and calculated spectra. It is possible that agreement between experimental and calculated spectra may be improved by sampling more molecular configurations. Future studies will take snapshots from ab initio molecular dynamics simulations to determine the degree to which fluctuations in atomic configurations affect the X-ray spectra.

The spectral signature of valence delocalization in the $Ru^{II}Ru^{III}$ complex remains clear following the identification of the low energy edge of the B feature in Figure 1d with the e_g feature of $Ru[NH_3]$ fragment (B_1 in Figure 9b). With the explicit solvent models the leading edge of the simulated spectrum is well aligned with the experimental data, and the spin populations in Table 4 for these models show that the unpaired electron is well localized on the $Ru[NH_3]$ fragment. Use of the implicit solvent model leads to a −0.5 eV shift in B relative to the shell model, which is correlated with spin populations of 0.75 and 0.25 for $Ru[NH_3]$ and Ru[CN], respectively. The spectral shift is attributed to a delocalization of the valence electrons that increases the charge

density at the Ru[NH_3] atom. The spectrum also broadens further since the Ru[CN] contribution shifts to higher energy as it oxidizes. In the case of the vacuum simulation, the B feature is further shifted to 2839.7 eV similar to the B feature in $[Ru(NH_3)_6]^{2+}$ at 2839.5 eV. The Mulliken population on the Ru[NH_3] fragment is 0.0 with the majority of the spin population residing on the Ru[CN] atom and CN^- bridging ligand. Consequently, the shift of the leading edge tracked by the red dashed curve in Figure 9a monitors the redistribution of electrons between the Ru atoms and over the bridging ligand. The experiments and simulations imply that $Ru^{II}Ru^{III}$ should be viewed as having localized valence electrons, and highlight the role of specific solvent–solute interactions in governing the electronic properties of this complex.

The degree of delocalization in these mixed valence complexes has been previously estimated using parameters derived from electrochemical, UV/vis, and Stark spectroscopy,(57, 59) The electronic spectroscopies are only indirectly sensitive to the delocalization of the valence electrons, and rely on mapping experimental results to a two state model.(57, 60) Transition metal L-edge measurements are directly sensitive to the valence of the metal because the energies of 2p orbitals respond to changes in the electron density at the metal center. The X-ray measurements employed here suggest that the electronic coupling between metal centers is quite weak due to the fact that the mixed-valence spectra are indistinguishable from the monomer spectra. For $Fe^{II}Ru^{III}$, TDDFT predicts that the B feature in the Ru L_3-edge shifts by −1.3 eV as when the electron localizes on the Ru center instead of the Fe center. We expect that a delocalization of 10% indicated by a decrease in the spin population at the Ru center would result in a spectral shift of ~0.1 eV. Given that dimer and monomer spectra are nearly indistinguishable, we conclude that our experimental and explicit solvent results are in good agreement with previous electro-absorption measurements.

5 Summary

In this article, we have shown that TDDFT provides a predictive tool for Ru L_3-edge XA spectroscopy. The simulations reproduce each of the features present in experimental spectra, and a difference density analysis of the transitions identifies the molecular origin of each of the spectral features. We have concluded that B3LYP is an ideal functional for simulating Ru L_3-edge spectra. After calibration of the energy axis, B3LYP predicts the energy positions of the experimental spectra with a RMSD of 0.26 eV. The B3LYP functional emerges as the best functional for simulating the CT features that arise from the mixing of Ru 4d and ligand orbitals. Our results show that TDDFT has the distinct advantage of being able to treat systems of low-symmetry and we identify ligand-specific CT features in the Ru L_3-edge spectra of $N3^{4-}$. We also demonstrate that TDDFT can successfully simulate Ru L_3-edge XA spectra of systems containing multiple metal centers when explicit solute–solvent interactions are taken into account. In the case of $Fe^{II}Ru^{III}$ and $Ru^{II}Ru^{III}$ complexes strong hydrogen bonding interactions with the CN ligands stabilize and localize the +2 oxidation state on the metal cyanide moiety, and the +3 oxidation state is observed on the ammine fragment. This study describes in detail how core-level excitations within TDDFT can be computed using many of the most widely used quantum chemistry codes providing a useful and powerful interpretive tool for equilibrium and ultrafast Ru L_3-edge spectroscopy.

‖ Author Present Address

University of Rochester, Department of Chemistry, RC Box 270216, Rochester, New York 14627-0216.

⊥ Author Present Address

Max Planck Research Department for Structural Dynamics at the University of Hamburg, 22607 Hamburg, Germany.

Acknowledgment

This work was supported by the Office of Basic Energy Sciences of the U.S. Department of Energy Grant No. DE-SC0002190 (B.V.K, S.L.D, C.B., and M. K.). M.K. acknowledges fellowship support from the David and Lucille Packard Foundation and the Alfred P. Sloan Foundation. The work at LBNL (N.H., M.L.S., H.C., and R.W.S.) was supported by the Director, Office of Science, Office of Basic Energy Sciences, the Chemical Sciences, Geosciences, and Biosciences Division under the Department of Energy, Contract No. DE-AC02-05CH11231. H.C. acknowledges the Basic Science Research Program 2009-0068446 and 2010-0006570 through the National Research Foundation of Korea funded by the Ministry of Education, Science and Technology, and N.H. acknowledges funding from the Max Planck Society and the University of Hamburg. A portion of the research was performed using EMSL, a national scientific user facility sponsored by the U.S. Department of Energy's Office of Biological and Environmental Research and located at Pacific Northwest National Laboratory (PNNL). PNNL is operated for the Department of Energy by the Battelle Memorial Institute under Contract DE-AC06-76RLO-1830. M.V. acknowledges support from by the U.S. Department of Energy's (DOE), Office of Basic Energy Sciences, Chemical Sciences program.

References

(1) Campagna, S.; Puntoriero, F.; Nastasi, F.; Bergamini, G.; Balzani, V. Photochemistry and Photophysics of Coordination Compounds: Ruthenium. Top. Curr. Chem. 2007, 280, 117−214.

(2) Grätzel, M. Recent Advances in Sensitized Mesoscopic Solar Cells. Acc. Chem. Res. 2009, 42, 1788−1798.

(3) Concepcion, J. J.; Jurss, J. W.; Brennaman, M. K.; Hoertz, P. G.; Patrocinio, A. O. T.; Murakami Iha, N. Y.; Templeton, J. L.; Meyer, T. J. Making Oxygen with Ruthenium Complexes. Acc. Chem. Res. 2009, 42, 1954−1965.

(4) Alperovich, I.; Smolentsev, G.; Moonshiram, D.; Jurss, J. W.; Concepcion, J. J.; Meyer, T. J.; Soldatov, A.; Pushkar, Y. Understanding the Electronic Structure of 4d Metal Complexes: From Molecular Spinors to L-Edge Spectra of a di-Ru Catalyst. J. Am. Chem. Soc. 2011, 133, 15786−15794.

(5) Shearer, J.; Callan, P. E.; Masitas, C. A.; Grapperhaus, C. A. Influence of Sequential Thiolate Oxidation on a Nitrile Hydratase Mimic Probed by Multiedge X-Ray Absorption Spectroscopy. Inorg. Chem. 2012, 51, 6032−6045.

(6) Gawelda, W.; Johnson, M.; de Groot, F. M. F.; Abela, R.; Bressler, C.; Chergui, M. Electronic and Molecular Structure of Photoexcited [RuII(bpy)3]2+ Probed by Picosecond X-Ray Absorption Spectroscopy. J. Am. Chem. Soc. 2006, 128, 5001−5009.

(7) Van Kuiken, B. E.; Huse, N.; Cho, H.; Strader, M. L.; Lynch, M. S.; Schoenlein, R. W.; Khalil, M. Probing the Electronic Structure of a Photoexcited Solar Cell Dye with Transient X-Ray Absorption Spectroscopy. J. Phys. Chem. Lett. 2012, 3, 1695−1700.

(8) Saes, M.; Bressler, C.; Abela, R.; Grolimund, D.; Johnson, S. L.; Heimann, P. A.; Chergui, M. Observing Photochemical Transients by Ultrafast X-Ray Absorption Spectroscopy. Phys. Rev. Lett. 2003, 90, 047403/1−047403/4.

(9) Stavitski, E.; de Groot, F. M. F. The CTM4XAS Program for EELS and XAS Spectral Shape Analysis of Transition Metal L Edges. Micron 2010, 41, 687−694.

(10) Alperovich, I.; Moonshiram, D.; Soldatov, A.; Pushkar, Y. Ru L2,3 Xanes Theoretical Simulation with DFT: A Test of the Core-Hole Treatment. Solid State Commun. 2012, 152, 1880−1884.

(11) Campbell, L.; Mukamel, S. Simulation of X-Ray Absorption near Edge Spectra of Electronically Excited Ruthenium Tris-2,2′-Bipyridine. J. Chem. Phys. 2004, 121, 12323−12333.

(12) Ekström, U.; Norman, P.; Carravetta, V. Relativistic Four- Component Static-Exchange Approximation for Core-Excitation Processes in Molecules. Phys. Rev. A 2006, 73, 022501.

(13) Ikeno, H.; Tanaka, I.; Koyama, Y.; Mizoguchi, T.; Ogasawara, K. First-Principles Multielectron Calculations of Ni L2,3 NEXAFS and ELNES for LiNiO2 and Related Compounds. Phys. Rev. B 2005, 72, 075123/075121−075123/075128.

(14) Wang, F.; Ziegler, T.; van Lenthe, E.; van Gisbergen, S.; Baerends, E. J. The Calculation of Excitation Energies Based on the Relativistic Two-Component Zeroth-Order Regular Approximation and Time-Dependent Density-Functional with Full Use of Symmetry. J. Chem. Phys. 2005, 122, 204103.

(15) Casarin, M.; Finetti, P.; Vittadini, A.; Wang, F.; Ziegler, T. Spin- Orbit Relativistic Time-Dependent Density Functional Calculations of the Metal and Ligand Pre-Edge XAS Intensities of Organotitanium Complexes: TiCl4, Ti(η5-C5H5)Cl3, and Ti(η5-C5H5)2Cl2. J. Phys. Chem. A 2007, 111, 5270−5279.

(16) Bast, R.; Jensen, H. J. A.; Saue, T. Relativistic Adiabatic Time- Dependent Density Functional Theory Using Hybrid Functionals and Noncollinear Spin Magnetization. Int. J. Quantum Chem. 2009, 109, 2091−2112.

(17) Lopata, K.; Van Kuiken, B. E.; Khalil, M.; Govind, N. Linear- Response and Real-Time Time-Dependent Density Functional Theory Studies of Core-Level Near-Edge X-Ray Absorption. J. Chem. Theory Comput. 2012, 8, 3284−3292.

(18) Vogler, A. ; Kissl inger, J. Photosubstitution of Pentaamminechlororuthenium(III) Hexacyanoruthenate(II) Following Outer-Sphere Intervalence Excitation. J. Am. Chem. Soc. 1982, 104, 2311−2312.

(19) Neese, F. The Orca Program System. WIREs: Comput. Mol. Sci. 2012, 2, 73−78.

(20) Becke, A. A New Mixing of Hartree-Fock and Local Density- Functional Theories. J. Chem. Phys. 1993, 98, 1372.

(21) Stephens, P. J.; Devlin, F. J.; Chabalowski, C. F.; Frisch, M. J. Ab Initio Calculation of Vibrational Absorption and Circular Dichroism Spectra Using Density Functional Force Fields. J. Phys. Chem. 1994, 98, 11623−11627.

(22) Weigend, F.; Ahlrichs, R. Balanced Basis Sets of Split Valence, Triple Zeta Valence and Quadruple Zeta Valence Quality for H to Rn: Design and Assessment of Accuracy. Phys. Chem. Chem. Phys. 2005, 7, 3297−3305.

(23) Klamt, A.; Schuurmann, G. Cosmo: A New Approach to Dielectric Screening in Solvents with Explicit Expressions for the Screening Energy and Its Gradient. J. Chem. Soc., Perkin Trans. 2 1993, 799−805.

(24) Adamo, C.; Barone, V. Toward Reliable Density Functional Methods without Adjustable Parameters: The PBE0Model. J. Chem. Phys. 1999, 110, 6158−6170.

(25) Dolg, M.; Wedig, U.; Stoll, H.; Preuss, H. Energy-Adjusted Ab Initio Pseudopotentials for the First Row Transition Elements. J. Chem. Phys. 1987, 86, 866−872.

(26) Berendsen, H. J. C.; Grigera, J. R.; Straatsma, T. P. The Missing Term in Effective Pair Potentials. J. Phys. Chem. 1987, 91, 6269−6271.

(27) Berendsen, H. J. C.; Postma, J. P. M.; van Gunsteren, W. F.; DiNola, A.; Haak, J. R. Molecular Dynamics with Coupling to an External Bath. J. Chem. Phys. 1984, 81, 3684−3690.

(28) Valiev, M.; Bylaska, E. J.; Govind, N.; Kowalski, K.; Straatsma, T. P.; Van Dam, H. J. J.; Wang, D.; Nieplocha, J.; Apra, E.; Windus, T. L.; et al. Nwchem: A Comprehensive and Scalable Open-Source Solution for Large Scale Molecular Simulations. Comput. Phys. Commun. 2010, 181, 1477−1489.

(29) Neese, F. Calculation of Electric-Field Gradients Based on Higher-Order Generalized Douglas-Kroll Transformations. J. Chem. Phys. 2005, 122, 204107.

(30) Pantazis, D. A.; Chen, X.-Y.; Landis, C. R.; Neese, F. All- Electron Scalar Relativistic Basis Sets for Third-Row Transition Metal Atoms. J. Chem. Theory Comput. 2008, 4, 908−919.

(31) Noro, T.; Sekiya, M.; Koga, T.; Saito, S. L. Relativistic Contracted Gaussian-Type Basis Functions for Atoms K through Xe. Chem. Phys. Lett. 2009, 481, 229−233.

(32) Becke, A. D. Density-Functional Exchange-Energy Approximation with Correct Asymptotic Behavior. Phys. Rev. A 1988, 38, 3098−3100.

(33) Perdew, J. P. Density-Functional Approximation for the Correlation Energy of the Inhomogeneous Electron Gas. Phys. Rev. B 1986, 33, 8822−8824.

(34) Tao, J.; Perdew, J. P.; Staroverov, V. N.; Scuseria, G. E. Climbing the Density Functional Ladder: Nonempirical Meta−Generalized Gradient Approximation Designed for Molecules and Solids. Phys. Rev. Lett. 2003, 91, 146401.

(35) Cohen, A. J.; Handy, N. C. Dynamic Correlation. Mol. Phys. 2001, 99, 607−615.

(36) van Lenthe, E.; Baerends, E. J.; Snijders, J. G. Relativistic Regular Two-Component Hamiltonians. J. Chem. Phys. 1993, 99, 4597−4610.

(37) Nichols, P.; Govind, N.; Bylaska, E. J.; de Jong, W. A. Gaussian Basis Set and Planewave Relativistic Spin−Orbit Methods in NWChem. J. Chem. Theory Comput. 2009, 5, 491−499.

(38) de Groot, F. M. F.; Hu, Z. W.; Lopez, M. F.; Kaindl, G.; Guillot, F.; Tronc, M. Differences between L3 and L2 X-Ray Absorption Spectra of Transition Metal Compounds. J. Chem. Phys. 1994, 101, 6570−6576.

(39) Sham, T. K. X-Ray Absorption Spectra of Ruthenium L Edges in Ru(NH3)6Cl3. J. Am. Chem. Soc. 1983, 105, 2269−2273.

(40) Hu, Z.; von Lips, H.; Golden, M. S.; Fink, J.; Kaindl, G.; de Groot, F. M. F.; Ebbinghaus, S.; Reller, A. Multiplet Effects in the Ru L23 X-Ray-Absorption Spectra of Ru(IV) and Ru(V) Compounds. Phys. Rev. B 2000, 61, 5262−5266.

(41) de Groot, F. M. F. Multiplet Effects in X-Ray Spectroscopy. Coord. Chem. Rev. 2005, 249, 31−63.

(42) Hocking, R. K.; Wasinger, E. C.; de Groot, F. M. F.; Hodgson, K. O.; Hedman, B.; Solomon, E. I. Fe L-Edge XAS Studies of K4[Fe(CN)6] and K3[Fe(CN)6]: A Direct Probe of Back-Bonding. J. Am. Chem. Soc. 2006, 128, 10442−10451.

(43) DeBeer George, S.; Petrenko, T.; Neese, F. Prediction of Iron K-Edge Absorption Spectra Using Time-Dependent Density Functional Theory. J. Phys. Chem. A 2008, 112, 12936−12943.

(44) Prendergast, D.; Galli, G. X-Ray Absorption Spectra of Water from First Principles Calculations. Phys. Rev. Lett. 2006, 96, 215502.

(45) Leetmaa, M.; Ljungberg, M. P.; Lyubartsev, A.; Nilsson, A.; Pettersson, L. G. M. Theoretical Approximations to X-Ray Absorption Spectroscopy of Liquid Water and Ice. J. Electron Spectrosc. Relat. Phenom. 2010, 177, 135−157.

(46) Sugiura, C.; Kitamura, M.; Muramatsu, S. X-Ray Absorption near-Edge Structure of Complex Compounds (NH4)3RhCl6, K3RuCl6, and Ru(NH3)6Cl3. J. Chem. Phys. 1986, 84, 4824−4827.

(47) Van Kuiken, B. E.; Khalil, M. Simulating Picosecond Iron KEdge X-Ray Absorption Spectra by Ab Initio Methods to Study Photoinduced Changes in the Electronic Structure of Fe(II) Spin Crossover Complexes. J. Phys. Chem. A 2011, 115, 10749−10761.

(48) Roemelt, M.; Beckwith, M. A.; Duboc, C.; Collomb, M.-N.; Neese, F.; DeBeer, S. Manganese K-Edge X-Ray Absorption Spectroscopy as a Probe of the Metal−Ligand Interactions in Coordination Compounds. Inorg. Chem. 2011, 51, 680−687.

(49) Reid, P. J.; Silva, C.; Barbara, P. F.; Karki, L.; Hupp, J. T. Electronic Coherence, Vibrational Coherence, and Solvent Degrees of Freedom in the Femtosecond Spectroscopy of Mixed-Valence Metal Dimers in H2O and D2O. J. Phys. Chem. 1995, 99, 2609−2616.

(50) Arnett, D. C.; Voehringer, P.; Scherer, N. F. Excitation Dephasing, Product Formation, and Vibrational Coherence in an Intervalence Charge-Transfer Reaction. J. Am. Chem. Soc. 1995, 117, 12262−12272.

(51) Doorn, S. K.; Dyer, R. B.; Stoutland, P. O.; Woodruff, W. H. Ultrafast Electron Transfer and Coupled Vibrational Dynamics in Cyanide Bridged Mixed-Valence Transition-Metal Dimers. J. Am. Chem. Soc. 1993, 115, 6398−6405.

(52) Lynch, M. S.; Van Kuiken, B. E.; Daifuku, S. L.; Khalil, M. On the Role of High-Frequency Intramolecular Vibrations in Ultrafast Back-Electron Transfer Reactions. J. Phys. Chem. Lett. 2011, 2, 2252− 2257.

(53) Lynch, M. S.; Slenkamp, K. M.; Khalil, M. Communication: Probing Non-Equilibrium Vibrational Relaxation Pathways of Highly Excited C ≡ N Stretching Modes Following Ultrafast Back-Electron Transfer. J. Chem. Phys. 2012, 136, 241101−241104.

(54) Wang, C. F.; Mohney, B. K.; Akhremitchev, B. B.; Walker, G. C. Ultrafast Infrared Spectroscopy of Vibrational States Prepared by Photoinduced Electron Transfer in (CN) 5FeCNRu(NH3)5 −. J. Phys. Chem. A 2000, 104, 4314−4320.

(55) Demadis, K. D.; Hartshorn, C. M.; Meyer, T. J. The Localizedto- Delocalized Transition in Mixed-Valence Chemistry. Chem. Rev. 2001, 101, 2655−2686.

(56) Blackbourn, R. L.; Hupp, J. T. Probing the Molecular Basis of Solvent Reorganization in Electron-Transfer Reactions. J. Phys. Chem. 1988, 92, 2817−2820.

(57) Vance, F. W.; Slone, R. V.; Stern, C. L.; Hupp, J. T. Comparative Absorption, Electroabsorption and Electrochemical Studies of Intervalence Electron Transfer and Electronic Coupling in Cyanide-Bridged Bimetallic Systems: Ancillary Ligand Effects. Chem. Phys. 2000, 253, 313−322.

(58) Kondov, I.; Vallet, V. r.; Wang, H.; Thoss, M. Ground- and Excited-State Properties of the Mixed-Valence Complex [(NH3)5RuIIINCRuII(CN)5]−. J. Phys. Chem. A 2008, 112, 5467−5477.

(59) Burewicz, A.; Haim, A. Formation and Properties of the Binuclear Complex (Pentaammineruthenium).μ.-Cyanopentacyanoferrate (1⁻). Inorg. Chem. 1988, 27, 1611−1614.

(60) Vance, F. W.; Karki, L.; Reigle, J. K.; Hupp, J. T.; Ratner, M. A. Aspects of Intervalence Charge Transfer in Cyanide-Bridged Systems: Modulated Electric Field Assessment of Distances, Polarizability Changes, and Anticipated First Hyperpolarizability Characteristics. J. Phys. Chem. A 1998, 102, 8320−8324.

DISCLAIMER